JTTEE5 9:463-477
© ASM International

A Study of the Microstructure of Yttria-Stabilized Zirconia Deposited by Inductively Coupled Plasma Spraying

In-Ha Jung, Ki-Kwang Bae, Myung-Seung Yang, and Son-Ki Ihm

(Submitted 14 February 2000)

Zirconia stabilized with 20 wt.% yttria was deposited to a thick free-standing type, ~7 mm, by (inductively coupled plasma spraying) (ICPS). The spheroidization of particles and the microstructure of deposits were analyzed. Spheroidization fraction dependence on spray parameters such as particle size, H_2 gas mixing quantity, and probe position was studied. Effects of parameters on the spheroidization of particles were analyzed by ANOVA (analysis of variance) (ANOVA). ANOVA results showed that the spheroidization fraction largely depend on H_2 gas mixing quantity and particle size, and there are also some dependence on probe position and H_2 gas mixing quantity. After melting, particles kept their chemical composition homogeneously from the center to their surface without segregation or evaporation. The degree of deformation of the diameter of the splat over the diameter of the spheroidized particle was approximately 320%, and splat thickness in the deposit varies between 2 μm and 3 μm depending on the deposition condition. The yttrium concentration gradient of the interlayer boundary appeared linear in the range of 0.5 to 1 μm. X-ray diffraction analysis and a transmission electron microscope (TEM) micrograph showed that low yttrium content particles resulted in tetragonal phase in deposit. The major characteristics of the microstructure of the thick free-standing deposit and solidification mode were studied. Microstructure of the bottom part of the deposit represented equiaxed or cellular structure. Equiaxed small grains prevailed when the droplets were quenched rapidly on substrate. The middle part of the deposit showed large columnar grains, of about 100 μm thick and 300 μm long. This may be due to high substrate or deposit temperatures and results in recrystallization and grain growth.

The effects of the parameters, such as H_2 gas mixing quantity, particle size, spraying distance, and probe position, on the microstructure of the deposits were evaluated. The H_2 gas mixing quantity of Ar/H_2 = 120/20 L/min compared to Ar/H_2 = 120/10 L/min resulted in larger grain size and thicker cellular in chill. Grain shapes were affected by the heat removal rate from the deposit to its surrounding. Deposition with larger particle size showed heterogeneous grain size, insufficient particle melting, and incomplete recrystallization. The effect of probe position was less than the others.

Keywords microstructure, solidification mode, TEM, thick deposit

1. Introduction

Plasma spraying was initially applied for corrosion resistance onto hard metal in the early 1900s.[1] The industrial applications have increased steadily in the chemical, automotive, aeronautic and space, electronic, ceramic, and nuclear fields, *etc.* fields. Thus far a number of studies have been devoted to new applications.

Plasma spraying is a combined process of high- temperature melting, quenching, and consolidation into a single operation, which often produces a rapidly quenched structure. Therefore, the characteristics of the deposit are fine microstructure, in which elements exhibit extended solubility and reduced segregation.[2] The plasma spraying technique uses range from corrosion-, temperature-, and abrasion-resistant coatings to the production of monolithic and near-net shapes of metallic and ceramic parts.[3]

Although plasma spraying offers a high quenching rate, annealing of the deposit occurs with the hot plasma and recalescence associated with solidification. During spraying by vacuum plasma spraying (VPS), the temperature of the deposit is very high and, thus, undergoes considerable self-annealing, altering the rapidly solidified structure.[4] This self-annealing can be beneficial, since it provides stress relief and recrystallization, while retaining fine grain size and solute supersaturation with the excellent wear and corrosion properties.[5]

In general, the thick and dense ceramic deposits are difficult to spray compared to metals due to the relatively high melting temperature and low thermal conductivity. Inductively coupled plasma spraying (ICPS) is expected to potentially provide new spraying technologies to produce thick ceramic deposits. In 1985, Jurewicz, Kaczmarek, and Boulos reported the first applications for induction plasma technology in the area of spraying metals and alloys.[6, 7] Jiang[8] has sprayed tungsten (T_m = 3680 K, C_p = 134 J/kg·k) powder by ICPS on a graphite substrate to fabricate a free-standing, thick deposit with more than a 90% theoretical density. He measured the substrate temperature as high as 2100 K during spraying and concluded that the density of the de-

---

In-Ha Jung, Korea Atomic Energy Research Institute, Yusong, Taejon, Korea, 305-353, and Department of Chemical Engineering, Korea Advanced Institute of Science and Technology, 373-1 Kuson-dong, Yusong-gu, Taejon, Korea, 305-701; **Ki-Kwang Bae** and **Myung-Seung Yang,** Korea Atomic Energy Research Institute; and **Son-Ki Ihm,** Department of Chemical Engineering, Korea Advanced Institute of Science and Technology. Contact e-mail: nihjung@nanum.kaeri.re.kr.

posit increased with temperature. He observed large columnar grains parallel to the heat removal direction.

ZrO_2 is usually applied for thermal barrier coating applications due to the high melting temperature, and Mg, CeO, and Y_2O_3 are often added to ZrO_2 for phase stabilization. Recently, stabilized ZrO_2 with additives (Y_2O_3, Al_2O_3, SiC, *etc.*) has been studied for the nuclear fuel industry as a matrix fuel due to its mechanical stability and neutron damage resistance.[9]

There are several different phase diagrams for the ZrO_2-Y_2O_3 system.[10,11] The high melting point characteristic causes difficulties in determining the phase diagram near the melting temperature. According to Srivastava *et al.*,[10] zirconia containing 5 to 10 mol.% of Y_2O_3 solidifies at 2970 K and maintains the cubic phase to 2200 to 02500 K. Then, the tetragonal *t*-phase transformation takes place depending on the yttrium contents. Finally, at 800 K, the martensitic transformation takes place to form a monoclinic phase. From 10 to 65 mol.% of Y_2O_3, a pure cubic phase is dominant to room temperature.

There are many factors influencing the plasma process outcome. One estimates the number of major parameters involved in the plasma spray process to be at least 35,[12] and another indicates that there are ~100 interrelated processing parameters influencing the particle temperatures, velocities, and the final quality of the coatings.[13] The influence of these parameters needs to be evaluated and the major parameters optimized.

Statistical methods greatly improve the efficiency of experiments, and, often, valuable conclusions can be drawn. In recent years, the value of statistical techniques that identify the interaction among the parameters and optimize those parameters have been evaluated useful, and subsequently employed by many thermal spray researchers to get the best performing coatings.[14–17]

In this paper, the parameters which that affect spheroidization particles were evaluated by ANOVA,[18] one of the statistical methods, and the microstructure of the free-standing deposit of zirconia stabilized with 20 wt.% yttria (yttria-stabilized zirconia (YSZ), sprayed by ICPS, was studied. The solidification of the deposit is categorized by five modes and they are analyzed. The microstructure of the YSZ thick deposit related to the spray parameters such as particle size, spray distance, and probe position is studied. The variations in the chemical composition of the spheroidized particles and layers of the deposit are measured by electron probe microanalysis (EPMA).

2. Experimental Procedure

Zirconia stabilized with 20 wt.% yttria (AMDRY146, fused and crushed, cubic, $T_m = 2970$ K, METCO, Westbury, NY) powder was used as feedstock. Table 1 shows the chemical composition in wt.% of yttrium and zirconium analyzed by inductively coupled plasma-atomic emission spectrometer (ICP-AES, model JY50P, JOBIN YVON, France). The feedstock was used in size cuts of –45, –75, and –90 μm. In this paper, a description of –45 μm means the powder sieved with ASTM No. 325, –75 μm with ASTM No. 200, and –90 μm with ASTM No.170. The average diameter of each powder is shown in Table 1. Particle size was measured by a particle size analyzer (MAE5000, MALVERN, United Kingdom).

Inductively coupled plasma spray of 100 kW, 300 kHz equipment was used. A cylindrical spraying chamber, 1.1 m diameter × 1.8 m length, with double walls and a water-cooling system is shown in Fig. 1. A volumetric powder feeder (CYLCO, Sylvester Company, OH) with an 8 thread/in. driving screw was used. The Ar gas was supplied as the powder carrier gas and the powder hopper was vibrated in order to feed the powder smoothly. The Ar gas was also used as the central gas, and H_2 with Ar was used as the sheath gas. Experimental conditions are summarized in Table 2.

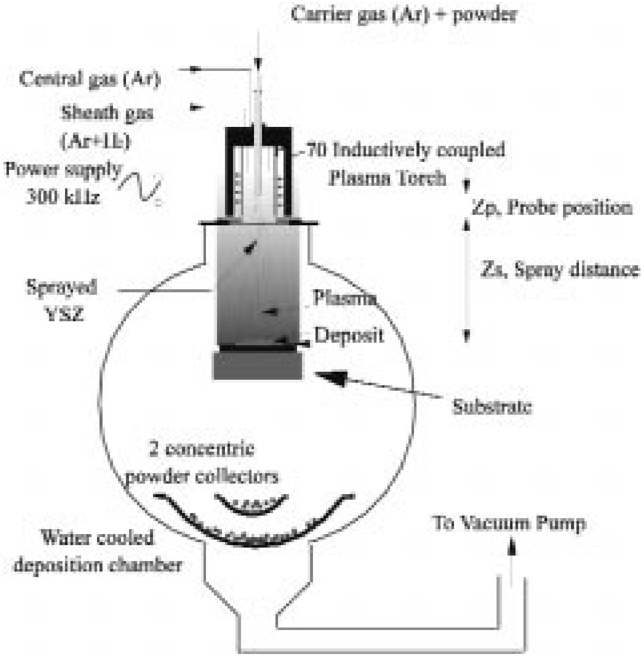

Fig. 1 Schematic drawing of the powder deposition equipment

Table 1 Chemical composition and average particle size of feedstock

Chemical composition (wt.%)			Particle size (μm)		
Y	Zr	O	–45	–75	–90
16.6	55.4	28	28	31.8	39

After evacuating the chamber to 50 Torr, the plasma was ignited and then the chamber pressure was adjusted to 200 Torr. To observe the degree of particle melting during spraying, a water bath of 280 mm diameter was laid on the bottom of the chamber. At the same time, a water bath of 130 mm diameter was overlapped on the 280 mm bath to study the variation of particle melting with distance from spray axis. The collected particles in the baths, the center, and surrounding bath were separately dried in an oven. Spheroidization fraction was then measured by counting the number of fully spheroidized particles over total observed number of particles. ANOVA was used to evaluate the interaction effects as well as the main effects on spheroidization.

To fabricate the deposits, a rectangular graphite bar, 25 × 25 × 40 mm, was used as a substrate. For thick deposits of ~7 mm, powder was sprayed in about 20 to 60 seconds. The speci-

Table 2 Summary of YSZ powder deposition conditions

	Parameters	Condition
Fixed parameters	Central gas flow rate, Ar (L/min)	35
	Powder feed rate (g/min)	16.6
	Carrier gas flow rate, Ar (L/min)	5
	Chamber pressure (Torr)	200
Variable parameters	Powder spraying distance, Z_s (cm)	22 and 30
	Sheath gas composition, G_{comp} (L/min)	120(Ar) + 10(H_2) and 120(Ar) + 20(H_2)
	Probe position, Z_p (cm)	4 and 8
	Particle size (μm)	−90, −75, and −45

Table 3 Result of powder spheroidization

Condition (80 kW, 200 Torr)		Spheroidization fraction(a)			
			Particle size (A)		
G_{comp} (C) (Ar/H_2, L/min)	Z_p (B) (cm)	Collect position	−45 μm	−75 μm	−90 μm
120/20	8	Center	. . .	98.01	. . .
		Surround	. . .	97.87	. . .
		Average	98.22	97.94	95.31
120/10	8	Center	. . .	90.14	. . .
		Surround	. . .	89.7	. . .
		Average	91.62	89.72	86.82
120/20	4	Center	. . .	93.7	. . .
		Surround	. . .	90.78	. . .
		Average	97.50	92.24	86.96
120/10	4	Center	. . .	90.04	. . .
		Surround	. . .	89.48	. . .
		Average	90.96	89.76	84.67

(a) $$\text{Spheroidization fraction} = \frac{\textit{number of spheroidized particles}}{\textit{total observed number of particles}} \times 100$$

mens were cooled in an Ar atmosphere for 30 minutes. The specimens were then separated from the substrate and cut vertically with a diamond saw (Isomet 2000, Buehler, Lake Bluff, IL, USA). The cut section of the deposit was etched by a 50% hydrogen fluoride solution heated to its boiling point.

Samples of splats were obtained by spraying the particles onto a 2 mm thick stainless steel plate fixed on a graphite substrate for a short time.

A scanning electron microscope (JEOL JSM 840A, Japan Electron Optics Ltd., Tokyo) and an optical microscope (Leitz METALLUX 3, Iowa, USA) were used to study the microstructure of the deposit. ICP-AES was used for the chemical composition analysis of the feedstock. Chemical composition of the spheroidized particles and deposits were measured by EPMA (model SXR, CAMECA, Paris, France) with a beam size of 1 μm. The phases are analyzed by x-ray diffraction (XRD) (x-ray diffractometer, MXP3A-HF, Mac Science, Ishikawa, Japan) using Cu $K_{\alpha 1}$ radiation with a graphite monochromator. The scanning angle was between 20 and 100° at intervals of 0.05° using a step counting time of 3 s. A transmission electron microscope (JEOL 2000 FX2 JEOL, Massachusetts, USA) was used to observe internal microstructure. Samples were prepared by mechanical thinning followed by ion milling.

3. Results and Discussion

3.1 Spheroidization of Particle

Table 3 shows the effects of H_2 gas mixing quantity (G_{comp}) and probe position from the torch bottom (Z_p) on the spheroidization of three different particle sizes. The other parameters, 80 kW of plasma power and 200 Torr of chamber pressure, were fixed. Each parameter was assigned two or three levels according to the experimental design procedure of ANOVA. This design provides the smallest number of experiments. The effect of a parameter is denoted by a capital letter, as shown in Table 3 and 4. Thus, "A" refers to the effect of parameter A (particle size), "B" refers to the effect of parameter B (Z_p), "C" refers to the effect of parameter C (G_{comp}), "AB" refers to the A and B interaction, *etc.* ANOVA enables comparison of the variance in the experimental data for each parameter with statistical probability tables. The mean squares of all parameters, their interactions, and the random error component are first calculated. The F-statistic for testing for any main effect or interaction is found by dividing the mean square for the main effect or interactions by the mean square error. Finally, the value of the F-statistic is compared with the tabulated "probability of significance." The value of the F-statistic exceeds the probability of significance at some confidence level, and then that parameter is viewed as being significant.[14]

In this experiment, G_{comp} varied in two levels, Ar/H_2 = 120/20 and 120/10 L/min, and Z_p was 8 and 4 cm. The spheroidization fraction was averaged from three runs. As shown in Table 3, spheroidization fraction decreased with increased particle size. The higher mixing quantity of H_2 gas resulted in a higher spheroidization fraction, and similarly higher probe position resulted in a higher spheroidization fraction. The variation of the spheroidization fraction along the radial direction from the spray axis was relatively small. This is due to the higher enthalpy of H_2 gas, and also the higher probe position in the torch makes the particles easier to melt. And the small particles are easy to heat for a short heat transport length from the surface. Figure 2 shows spheroidized particles of −75 μm and its feed powder.

Table 4 shows the analyzed result by ANOVA on spheroidization fraction. The reliability of the model, that the effects of particle size (A), probe position (B), H_2 gas mixing quantity (C), and their interactions are reflected on the results of the spheroidization, shows 99% (Table 4, "Pr > F" on the third line from the top, reliability = 1 "Pr > F," Ref 18). Parameters A and C affect the result with 99% reliability, the higher F-statistic of effect C has more of an influence than parameter A, and the effect of parameter B is lower than the others. The interaction between parameters B and C (B∗C in Table 4) affects more than other interactions. This indicates that the result largely depends on parameters C and A, and there is a relationship between parameters B and C. Therefore, when altering the H_2 gas-mixing rate is considered, altering the probe position should also be considered.

From the calculated value of R-square, three parameters contribute about 80% to the results, and experimental error or other parameters, which are not reflected in the experimental design, are responsible for the other 20%.

From Table 4, strength of association, ω^2 (for A, $\omega_A{}^2 = \frac{SS_A - DF_A \times MS_E}{SS_T + MS_E} = \frac{235.8 - 2 \times 7.4}{866.6 + 7.4} = 0.253$), is calculated

Table 4 ANOVA result of the spheroidization experiment

```
General linear models procedure
   Dependent variable: spheroidization %
   Source            DF       Sum of squares          Mean square        F value      Pr > F
   Model             11       688.87478056            62.62498005        8.46         0.0001
   Error             24       177.74093333             7.40587222
   Corrected total   35       866.61571389

      R-square       CV           Root MSE       Mean of spheroidization %
      0.794902       2.961976     2.72137322     91.87694444

   Source            DF       Type I SS               Mean square        F value      Pr > F
   A                  2       235.78453889            117.89226944       15.92        0.0001
   B                  1        84.21121111             84.21121111       11.37        0.0025
   A*B                2        31.39840556             15.69920278        2.12        0.1420
   C                  1       286.23000278            286.23000278       38.65        0.0001
   A*C                2         4.25150556              2.12575278        0.29        0.7530
   B*C                1        31.24810000             31.24810000        4.22        0.0510
   A*B*C              2        15.75101667              7.87550833        1.06        0.3610

Duncan's multiple range test for variable: spheroidization %
   Alpha = 0.05          df = 24        MSE = 7.405872
   Number of means          2               3
   Critical range       2.293           2.408

Means with the same letter are not significantly different.
   Duncan grouping      Mean      N      A
      A                 94.574    12     1
      A
      A                 92.618    12     2
      B                 88.438    12     3

T-test procedure
   Variable: spheroidization %
      B          N        Mean            Std dev        Std error      Minimum         Maximum
      1          18       93.40638889     4.77353113     1.12513208     83.33000000     100.00000000
      2          18       90.34750000     4.82049737     1.13620213     79.63000000      98.17000000

   Variances       T           DF          Prob > |T|
   Unequal         1.9130      34.0        0.0642
   Equal           1.9130      34.0        0.0642
   For H0: Variances are equal, F′ = 1.02 DF = (17,17) Prob >  F′ = 0.9683

   Variable: spheroidization %
   C             N        Mean            Std dev        Std error      Minimum         Maximum
   1             18       94.69666667     4.80492976     1.13253281     79.63000000     100.00000000
   2             18       89.05722222     3.32460313     0.78361647     82.93000000      94.50000000

   Variances       T           DF          Prob > |T
   Unequal         4.0949      30.2        0.0003
   Equal           4.0949      34.0        0.0002
   For H0: variances are equal, F′ = 2.09     DF = (17,17) Prob > F′ = 0.1388
```

for parameters A, B, C, and shows $\omega_A^2 = 0.253$, $\omega_B^2 = 0.088$, and $\omega_C^2 = 0.319$, respectively. These results mean that parameter C affects the results of the spheroidization as much as by about 32%, parameter A 25.3%, *etc.* Through Duncan's multiple range test for parameters, whether the degree of melting is influenced by particle size is assessed. In the results of this test, there is some difference between –45 and –90 μm and –75 and –90 μm particles, but –45 and –75 μm are close together. This indicates that particle sizes below –75 μm are proper to melt in the range of these experimental conditions. The difference of average between the experimental levels and the identity of their variance was assessed by a *t*-test. Two different experimental levels of parameter C gave distinctively different results on spheroidization with 99.97% reliability, and parameter B showed 93.6%. Therefore, a preferential method for increasing spheroidization would be increasing the H_2 gas quantity.

3.2 Yttrium Concentration Profile of Spheroidized Particles

The variations in the concentration inside the spheroidized particles are listed in Tables 5 and 6. The concentration of spheroidized particles was measured with a 2 μm interval to radial direction from the center to the surface by 1 μm probe size (Table 5), or two or three points were measured for one particle (Table 6). Table 5 shows the concentration of yttrium for one particle

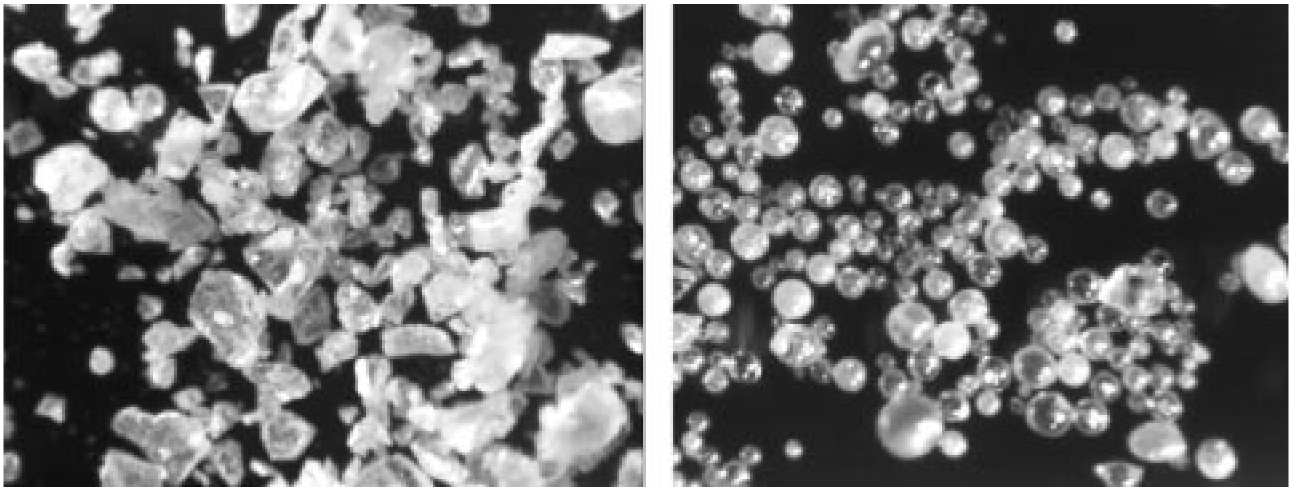

Fig. 2 Particle shape of feedstock (left) and spheroidized powder (right). (Spheroidization condition: Ar/H_2 = 120/20 L/min, plasma power = 80 kW, Z_p = 8 cm, and particle size = –75 μm)

Table 5 The concentration profile of a spheroidized particle by EPMA (particle diameter 37 μm, detection points 18)

Detection point	Y, wt.%	Zr, wt.%
1	16.52	59.73
2	16.12	59.46
3	16.06	58.68
4	16.63	58.90
5	16.42	58.55
6	16.31	59.34
7	18.52	58.98
8	16.58	58.42
9	17.35	59.15
10	16.66	58.05
11	16.38	58.46
12	16.64	58.25
13	16.64	58.4
14	16.95	58.71
15	16.98	58.58
16	16.46	58.42
17	17.41	57.86
18	16.09	58.81
Average	16.70	58.71
Standard deviation	0.59	0.49

Table 6 Average concentration of yttrium and zirconium for each particle (number of particles is 21)

Particle ID	Y, wt.%	Zr, wt.%
1	6.28	68.41
2	20.34	55.48
3	19.87	54.91
4	10.31	63.74
5	19.93	55.07
6	21.07	54.04
7	20.03	54.59
8	19.61	54.69
9	19.64	55.23
10	6.82	66.84
11	18.3	56.57
12	20.24	55.20
13	16.97	56.60
14	8.38	66.09
15	10.65	63.94
16	17.37	57.43
17	18.58	54.99
18	19.76	55.40
19	15.61	58.87
20	17.40	57.40
21	18.30	55.47
Average	16.45	58.14
Standard deviation	4.82	4.61

of about 37 μm diameter, and Table 6 for 21 particles. There was no concentration difference in the radial direction within a particle. This suggests that zirconia and yttria (T_m = 2700 K), although their melting points are different, are deposited without separation during spraying, while the concentration is different from particle to particle, as shown in Table 6. This may come from the manufacturing process of the particles. The concentrations of the feed powder (Table 1) and the spheroidized particle (Tables 5 and 6) are in good agreement.

3.3 Diameter and Thickness of Splat

Table 7 represents the average diameter of the spheroidized particles of three different particle sizes of –45, –75, and –90 μm. The average diameters of the feed powder and spheroidized particle are in good agreement, though the average diameter of feed powder is slightly smaller. The thickness of the splat was measured directly and averaged from several areas of cut sections of the deposit of about 7 mm. The splat thickness was 2 to 3 μm depending on the particle diameter. The average splat diameter was then calculated from the observed thickness of the splats as 100 to 130 μm. There exists about 5% difference in splat diameter between calculated and observed data. The degree of deformation of the diameter of the splat over the diameter of the spheroidized particle was approximately 320%. Figure 3 shows the splat samples with –75 μm particles. The splats have many cracks due to the rapid cooling.

Peer Reviewed

Table 7 Average diameter of the feedstock and spheroidized particle

Classification	Diameter of feedstock (μm)	Diameter of spheroidized particle (μm)	Splat thickness (μm)	Splat diameter (μm)	Degree of (%) deformation (a) (μm) (%)
–45 μm	28	31	1.97	100	323
–75 μm	31.8	34	2.14	110	324
–90 μm	39	41	2.7	130	317

Spraying condition: Ar/H_2 = 120/20 L/min, chamber pressure 200 Torr, Z_p = 8 cm, and Z_s = 22 cm

(a) Degree of deformation (%) = $\frac{splat\ diameter}{spheroidized\ particle\ diameter} \times 100$

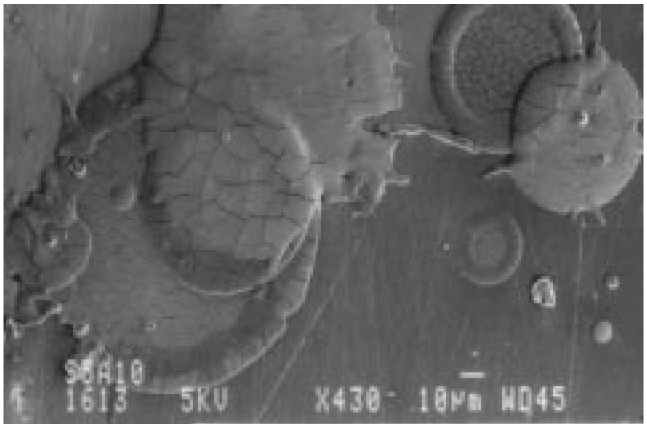

Fig. 3 Microstructure of the splats (spraying condition: particle size –75 μm, Ar/H_2 = 120/20 L/min, chamber pressure 200 Torr, Z_p = 8 cm, and Z_s = 22 cm)

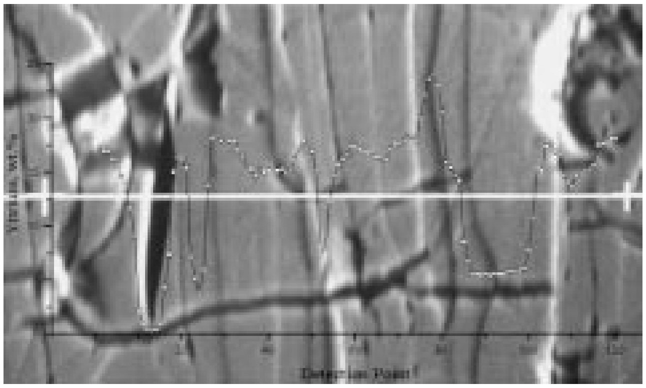

Fig. 4 Yttrium concentration profile through the layers (deposition condition: particle size –75 μm, Ar/H_2 = 120/20 L/min, chamber pressure 200 Torr, Z_p = 8 cm, and Z_s = 22 cm; average concentration 14.47 wt.%, standard deviation 4.64 wt.%, maximum concentration 23.99 wt.%, and minimum concentration 3.75 wt.%; and measuring distance 43 μm, sampled volume 7 mm, and beam size 1 μm)

3.4 Yttrium Concentration Profile of the Splats in Deposit

Figure 4 is a scanning electron micrograph of the lower bottom part of a deposit (particle size –75 μm, Ar/H_2 = 120/20 L/min, chamber pressure 200 Torr, Z_p = 8 cm, Z_s = 22 cm, and sample thickness 7 mm). The average thickness of the splats in the deposit was measured as 2.7 μm, which indicates that the degree of deformation during solidification was smaller than in other areas of average thickness of 2.14 μm (Table 7). This will be discussed in Section 3.8. Table 8 lists the yttrium concentration profile of Fig. 4 through the layers for a distance of 43 μm with 120 points. The average concentration of yttrium along the measured length in Fig. 4 represents 14.47 wt.% (excluding the large pore on the left), and the standard deviation is 4.64 wt.%. The reason for the discrepancy with the average concentration of spheroidized particles of 16.45 wt.% (Table 6) is that this section contains lower yttrium concentration layers of 4 to 7 wt.% (refer to Section 3.2). However, the concentration gradient of the interlayer boundary is linear in the range of 0.5 to 1 μm, although the particles have a discrete concentration. This implies that atoms in the newly deposited bottom surface of the splat diffuse to the previously deposited top surface at a short range, and liquid in the upper part of the splat solidifies massively in its own concentration.

3.5 Yttrium Concentration Profile at Grain Boundary

Figure 5 shows the concentration profile through the grain boundary for a distance of 8.9 μm with 18 points. The average yttrium concentration was 19.11 wt.%, a standard deviation 0.45 wt.%, a maximum concentration of 19.83 wt.%, and a minimum concentration of 18.08 wt.%. This result shows that the concentration fluctuation through the grain boundary is very small and that no segregation appears. Table 9 shows the concentration profile at the grain boundary for the material examined in Fig. 5.

3.6 Yttrium Concentration Profile of Chill

The microstructure and yttrium concentration profile for an 11 μm distance of chill (the fastest solidified part contact on the substrate) structure is represented in Fig. 6 and Table 10. The average yttrium concentration on the marked line shows 19.14 wt.%, a standard deviation of 0.36 wt.%, a maximum concentration of 19.95 wt.%, and a minimum concentration of 18.38 wt.%. From this result, the concentration profile during chilling shows

Table 8 Concentration of yttrium by EPMA qualitative analysis (for Fig. 4, measuring distance 43 μm, 120 points)

Detection point	Y, wt.%	Detection point	Y, wt.%	Detection point	Y, wt.%
1	17.27	41	15.31	81	15.97
2	16.87	42	15.22	82	15.48
3	16.91	43	15.26	83	14.65
4	16.25	44	14.94	84	14.22
5	16.06	45	15.11	85	8.58
6	14.55	46	16.20	86	6.76
7	13.80	47	17.27	87	5.69
8	11.69	48	17.88	88	5.66
9	9.0	49	17.62	89	5.51
10	2.196	50	16.93	90	5.53
11	0.92	51	15.08	91	5.49
12	0.51	52	8.44	92	5.55
13	0.38	53	7.53	93	5.65
14	0.45	54	12.27	94	5.67
15	0.89	55	14.65	95	5.82
16	4.29	56	15.80	96	5.91
17	7.38	57	16.23	97	5.83
18	15.05	58	16.82	98	6.03
19	16.32	59	17.34	99	6.12
20	16.38	60	17.44	100	7.90
21	15.45	61	17.23	101	10.90
22	7.22	62	16.97	102	15.43
23	5.13	63	16.85	103	15.20
24	3.75	64	17.08	104	17.45
25	6.0	65	16.48	105	17.88
26	13.69	66	16.29	106	16.93
27	18.11	67	16.09	107	16.72
28	18.29	68	17.23	108	14.66
29	17.98	69	17.52	109	14.13
30	18.09	70	17.74	110	13.76
31	17.97	71	18.31	111	14.72
32	18.03	72	18.58	112	14.96
33	17.21	73	18.30	113	15.15
34	16.56	74	17.97	114	15.37
35	15.61	75	20.07	115	15.66
36	15.29	76	22.25	116	17.51
37	14.70	77	23.64	117	17.67
38	15.38	78	23.99	118	17.81
39	15.05	79	23.01	119	18.19
40	15.21	80	20.68	120	18.16

Table 9 Yttrium concentration profile at the grain boundary by EPMA qualitative analysis (for Fig. 5, measuring distance 8.9 μm, 18 points)

Detection point	Y, wt.%	Detection point	Y, wt.%	Detection point	Y, wt.%
1	18.44	7	19.11	13	18.63
2	19.25	8	18.86	14	19.12
3	19.83	9	19.36	15	18.98
4	19.66	10	19.75	16	19.43
5	19.20	11	18.95	17	19.41
6	18.75	12	19.27	18	18.08

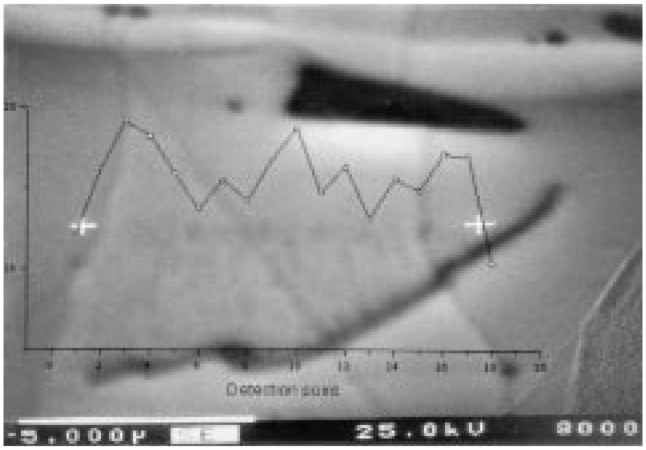

Fig. 5 Yttrium concentration profile at the grain boundary by EPMA (deposition condition: particle size –75 μm, Ar/H_2 = 120/20 L/min, chamber pressure 200 Torr, Z_p = 8 cm and Z_s = 22 cm; average concentration 19.11 wt.%, standard deviation 0.45 wt.%, maximum concentration 19.83 wt.%, and minimum concentration 18.08 wt.%; and measuring distance 8.9 μm, sampled volume 7 mm, and beam size 1 μm)

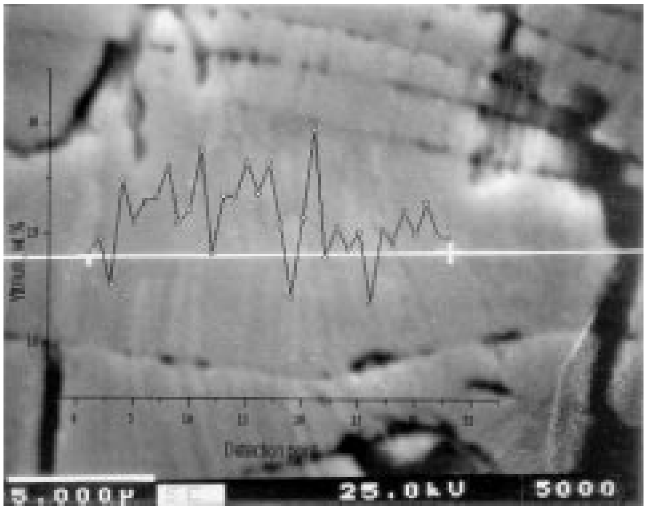

Fig. 6 Yttrium concentration profile of chill by EPMA (deposition condition: particle size –75 μm, Ar/H_2 = 120/20 L/min, chamber pressure 200 Torr, Z_p = 8 cm, and Z_s = 22 cm; average concentration 19.14 wt.%, standard deviation 0.36 wt.%, maximum concentration 19.95 wt.%, and minimum concentration 18.38 wt.%; and sampled volume 7 mm and beam size 1 μm)

neither yttrium concentration deviation nor segregation, which is the same as the behavior exhibited at the grain boundary.

3.7 XRD Analysis

For XRD analysis of a deposit, the modeling condition by Rietveld[19] was based on the relative concentration of yttria as 13.2 mol.% (16.5 wt.% yttrium), which is the same as the result of EPMA quantitative analysis of spheroidized particles (Table 6). Quality factors of the fitting, R_{wp} = 9.92 and χ^2 = 5.28, showed the high reliability of the refinement. Figure 7 represents both the model and experiment results. It shows that about 3% of the tetragonal phase, as shown in the small window in Fig. 7, with a lattice parameters of a = 3.614(1) and, c = 5.124(4), is contained in cubic matrix with a = 5.1430(2). The existence of a small tetragonal phase agrees with the results of EPMA quantitative

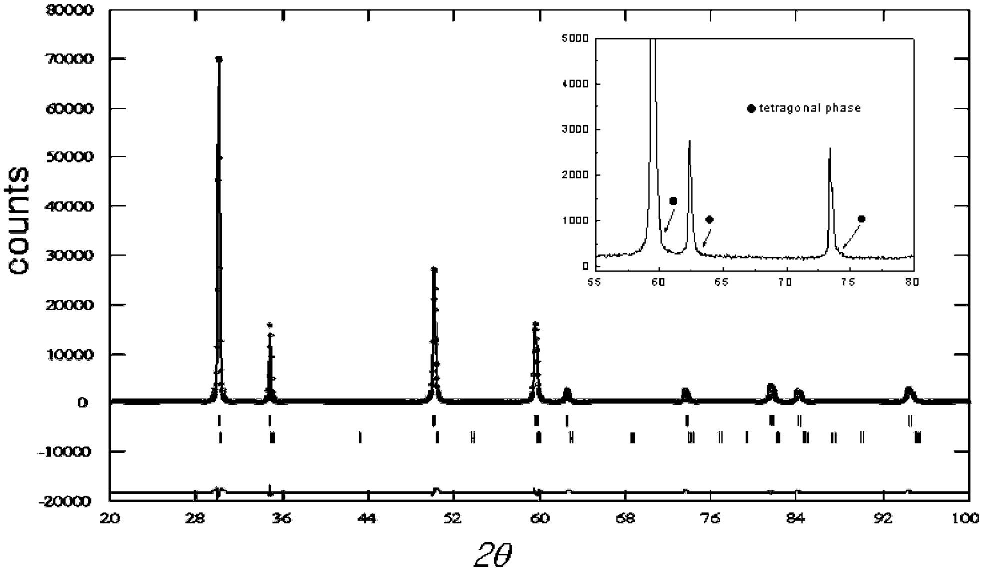

Fig. 7 X-ray diffraction pattern of a deposit (experimental (*) and modeled (—))

Table 10 Yttrium concentration profile on chill (for Fig. 6, measuring distance 11 μm, 33 points)

Detection point	Y, wt.%	Detection point	Y, wt.%	Detection point	Y, wt.%
1	18.84	12	18.82	23	19.06
2	18.96	13	19.35	24	18.87
3	18.53	14	19.36	25	19.02
4	19.49	15	19.66	26	18.38
5	19.10	16	19.38	27	19.04
6	19.30	17	19.65	28	18.93
7	19.32	18	19.10	29	19.23
8	19.61	19	18.43	30	18.99
9	19.11	20	19.16	31	19.30
10	19.21	21	19.95	32	18.99
11	19.76	22	18.79	33	18.98

analysis on the spheroidized particle described in Sections 3.2 and 3.4, because a tetragonal phase is stable at low yttrium contents. Figure 8 represents a TEM micrograph of the tetragonal phase and its index. Low yttrium content results in tetragonal phase. The t-ZrO$_2$ is identified by the week (211) superlattice-type reflections. Reflections of the type (100) and (110) disappear for the t-ZrO$_2$ but appear by multiple diffraction.[20]

3.8 Microstructure of the Deposit and Solidification Mode

The microstructure of the deposit by ICPS is characterized as a lamellae structure perpendicular to the spraying direction with columnar grains. Figure 9 is the schematic drawing based on the observed results in this experiment. This schematic drawing represents characteristics of the five parts of the deposit from bottom to top. In the bottom part, equiaxed and cellular grains, a "brick wall" named by Sampath and Herman,[21] pores, and cracks can be seen. In the lower middle part, columnar grains through a few layers, interlayer pores, and cracks are characteristic. In the middle part, relatively regular-sized columnar grains through many layers with excellent bonding and a dense microstructure can be seen. In the upper middle and top parts, the microstructure has the same characteristics as the middle part, but the sizes of columnar grain are irregular.

The following are descriptions of the characteristics' deposits by sectioning to the coating into five parts from the bottom to the top, as shown in Fig. 9.

Characteristics of the Bottom Part of Deposit. The shape of the layer depends on the ability to adhere by impact and deformation on the substrate or previously solidified splat.[22] In this experiment, the layers are not homogeneous, which may come from different particle size, temperature, velocity, *etc.* However, the bottom layer in contact with the graphite substrate generally shows fine-grained equiaxed and cellular grains separated by a horizontal gap, due to the poor contact between layers, and vertical cracks, as shown in Fig. 10. The brick wall is also observed.[21] A fine-grained equiaxed microstructure is observed in other literature.[23] They explained that the formation of such a microstructure inside the layers was favored by the low rate of heat removal at the interface to the substrate or previously deposited layer, affected by contact morphology and, thus, by the increase of thermal contact resistance. Moreau *et al.*[24] suggested that the inclusions of entrapped air gaps delay heat removal, making the formation of an equiaxed microstructure more probable than a columnar structure.

Meanwhile, Bhat and Herman[25] observed very fine crystals of bcc iron on a force-quenched substrate by liquid nitrogen. They interpreted the appearance of fine crystals as super undercooling of the droplets rather than thermal contact resistance, as was the conclusion of Sampath *et al.*[4] An increase in temperature difference between the droplet and the substrate results in more nuclei of fine grains.[26] In this experiment, the bottom layer was deposited at first on a cold substrate before being heated by the droplets or plasma flame. Therefore, it is easy for the liquid

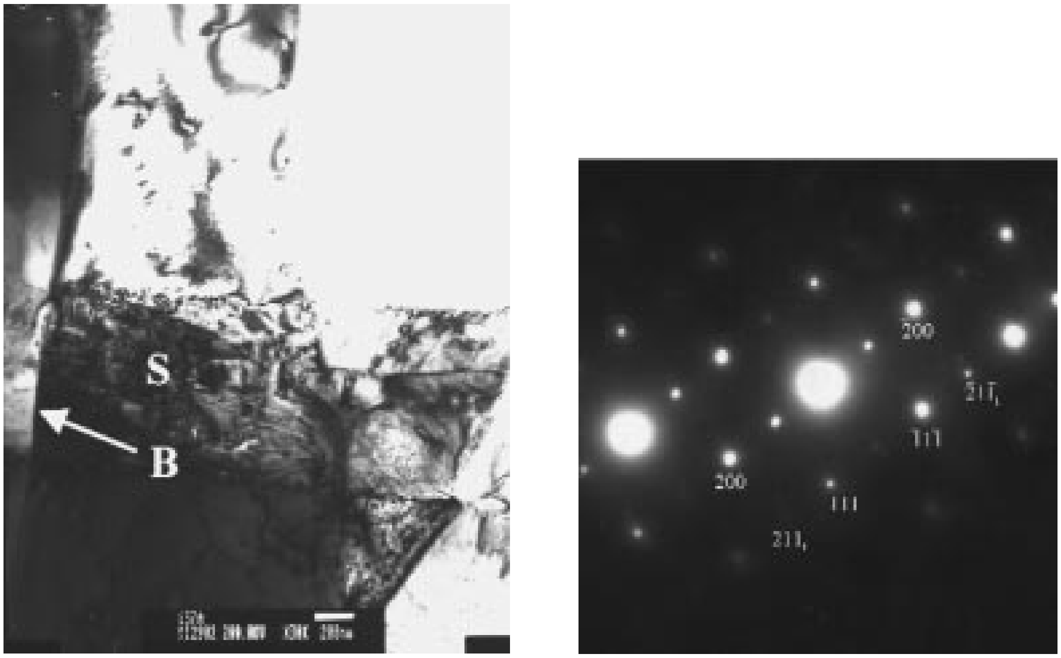

(a) (b)

Fig. 8 Microstructure of the columnar grain through the layers and diffraction pattern. (**a**) "B" is the grain boundary through the layers, and "S" is a layer of the tetragonal phase. (**b**) Index of the diffraction pattern of S. (Deposition condition: particle size-–75 μm, Ar/H_2 = 120/20 L/min, chamber pressure 200 Torr, Z_p = 8 cm, and Z_s = 22 cm)

droplets to be super-quenched and the effect should be large in the case of a thin splat. In this condition, especially in thin layers, a high concentration of nucleation results in equiaxed grains, as shown in Fig. 10. Cellular or cell structure is subject to be generated at higher temperature. As shown in Fig. 11, equiaxed small grains are mostly in the thin layers and cellular grains are in the thick layers. Many cellular grains are grown through the layers when they contact and solidify, as shown in Fig. 12.

Characteristics of the Lower Middle Part of Deposit. As the deposit layers are built up, the temperatures of the substrate and deposit increase due to the heat from the molten droplet and thermal fluxes coming from the plasma torch. The temperature is still low but higher than the bottom part. This is related to the low thermal conductivity of ZrO_2 (4 W/m K, Ref 27) in comparison to graphite (160 W/m K). The temperature difference between the bottom and upper parts generates residual stress during solidification and cooling. Finally, it results in thermal cracks in the deposit.[28] According to Pawlowski,[28] the residual stresses can be accumulated by (1) quenching stresses, generated during solidification; (2) phase transformation stresses; and (3) cooling stresses, generated while the sprayed specimen cools down after processing. The cracks inside the layers are generated resulting from the relaxation of those residual stresses.[29] The cracks in this sample might come from all three factors, as Pawlowski described above. The cracks were generally located along the layer and grain boundaries. However, most layer boundaries are well bonded, as shown in Fig. 13 (in this figure, faint layer boundary lines can be seen). The liquid phase between the layers accelerates the bonding characteristics, when a new splat starts to solidify. The source of the liquid phase may be liquid, which remains in the previously deposited layer surface, or liquid remelted by the heat of the new droplet. Figure 14 is a fractured surface of this sample and shows a perfect bonding structure between splats. Strong adhesion of the contact area between the splats may result from physical and metallurgical interaction mechanisms.[30]

Characteristics of the Middle Part of the Deposit. No boundary lines between layers are observed in the middle part of the deposit, and the grain shape is large columnar through the layers, as shown in Fig. 15. Grains are thicker and longer than the lower middle part, and some of the columnar grains reached 100 thick and 300 μm long. The grain size is more homogeneous than in the other parts of the deposit. Neither cracks nor interlayer pores can be seen. This is due to the high temperature with continued spraying. The droplet heat, latent heat of solidification (recalescence effect), and retarding heat removal by low thermal conductivity result in increasing the deposit temperature. As previously mentioned, Jiang[8] observed substrate temperatures reaching 2100 K during spraying by ICPS. Following Kurz and Fisher,[26] the solid/liquid interface grows as a planar front and partial recrystallization can occur when the deposit temperature is high and homogeneous.

It is well known that there are two stages of recrystallization.[31] Primary recrystallization is the process by which nucleation and growth of strain-free grains occurs in a matrix that has been plastically deformed. The second is the process that a few large grains grow at the expense of fine grains. The driving force for primary recrystallization is the energy in the matrix, which comes from plastic deformation during the droplet deformation and internal defects during solidification. The stored energy is of the order of 0.5 to 1 cal/g.[32] Although this is small, it provides sufficient energy to move the grain boundary and increase the

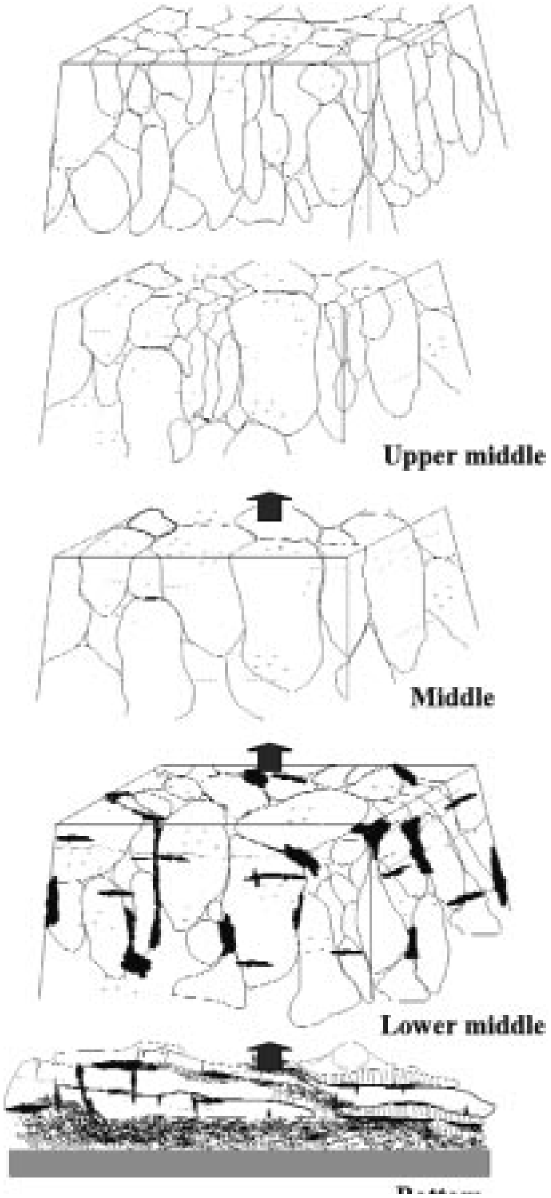

Fig. 9 Schematic drawing of deposition by sectioning into five parts from bottom to top of the deposit

grain size. At higher temperature, the grain growth follows recrystallization, so that larger grains can be observed.[32] Kim *et al.*[33] and Sampath *et al.*[2] have observed similar two-stage recrystallization and no trend of chemical separation in the plasma-sprayed deposits. Craig and Hideaki[34] suggests that a structural relaxation mechanism takes place more easily with the help of many defects, such as stresses and/or oxygen vacancies.

Grains in this experiment grow large columnar through the splat layers parallel to the heat removal direction. Sampath *et al.*[4] observed a columnar grain structure with zirconia-8 wt.% yttria, but the grains were bounded by the layer boundaries. This might be due to the low substrate or deposit temperature of the APS process and quick solidification without grain growth.

Fig. 10 Microstructure of bottom layer contact to the substrate (chill, equiaxed, and cellular grains)

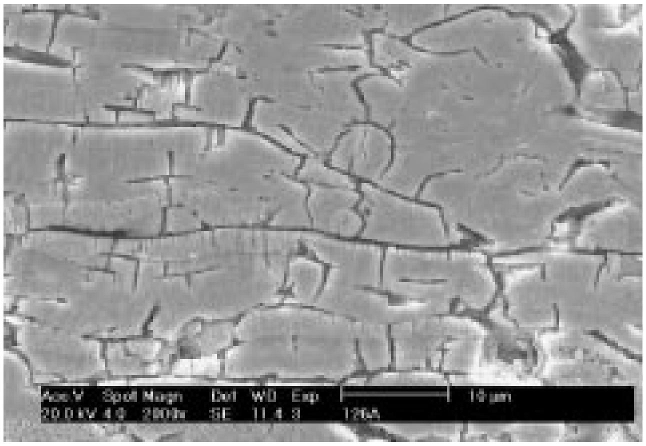

Fig. 11 Microstructure of the bottom part (equiaxed small grains on thinner layer and cellular on thick)

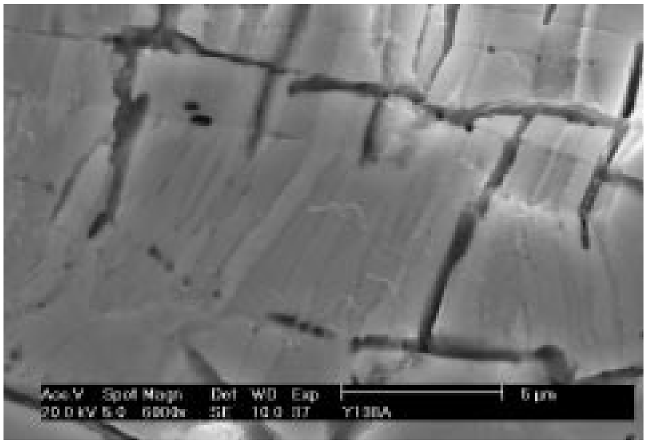

Fig. 12 Microstructure of the bottom part (cellular grains grown through the layers)

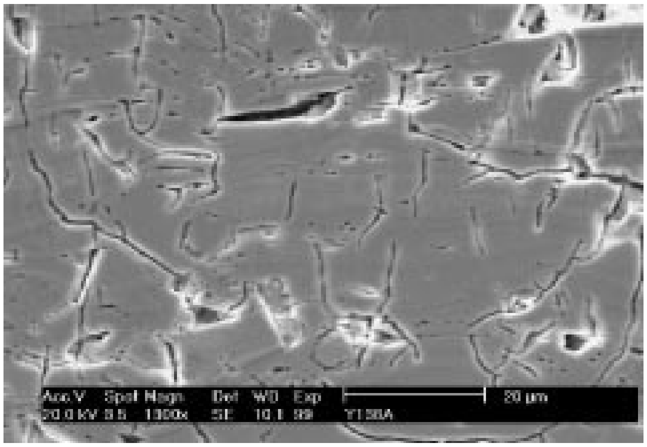

Fig. 13 Microstructure of the lower middle part (cracks, intralayer pores, and strong bonded layers)

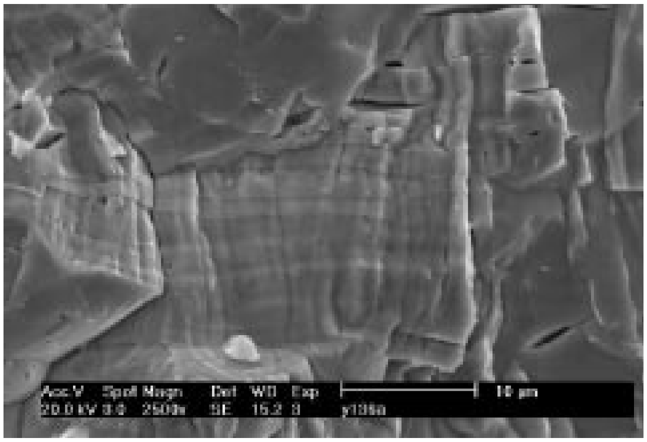

Fig. 14 Microstructure of a fractured surface (strong bond between layers)

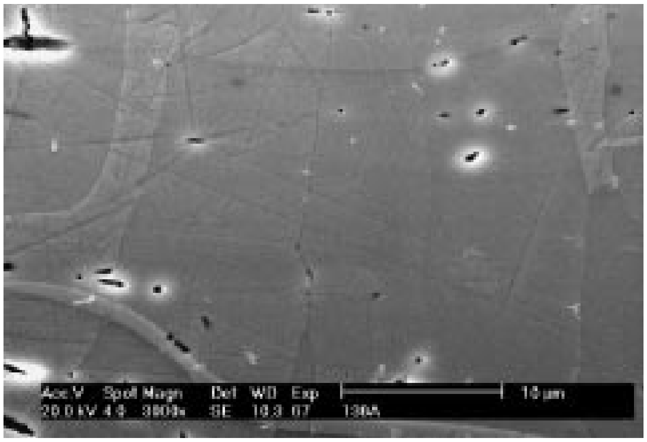

Fig. 15 Microstructure of the middle part of a deposit

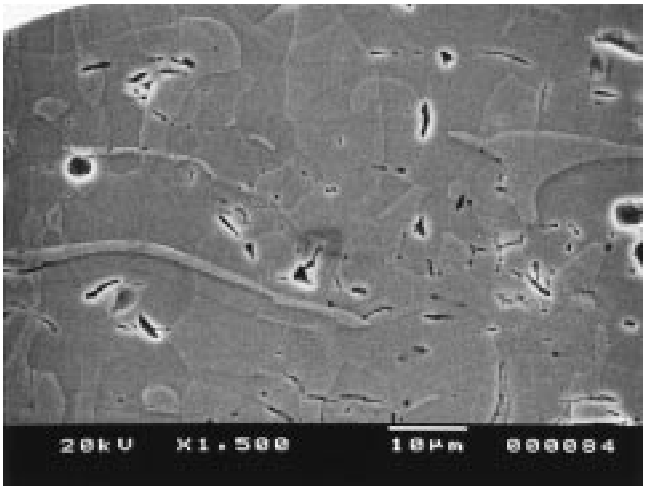

Fig. 16 Microstructure of the upper middle part of a deposit

Fig. 17 Microstructure of the initial stage recrystallization (deposition condition: particle size –75 μm, Ar/H_2 = 120/20 L/min, Z_p = 8 cm, Z_s = 30 cm, and chamber pressure 200 Torr)

Characteristics of the Upper Middle and Top Part of the Deposit. The shapes of the grain and deposited layer of these parts of the coating are the same as the middle part, but the grain size was not uniform due to insufficient time for recrystallization, as shown in Fig. 16. However, droplet flattening and interlayer adhesion are excellent; thus, these parts of the coating also represent low porosity and cracks. Figure 17 shows the initial microstructure stage of recrystallization, which is also evident at the top part of the deposit.

3.9 Effect of Parameters on Microstructure of Deposit

Particle size. The thickness and length of the columnar grain, shape of the grain, as well as thickness of the layers exhibit a wide range, which depends on the particle size. Particle size and

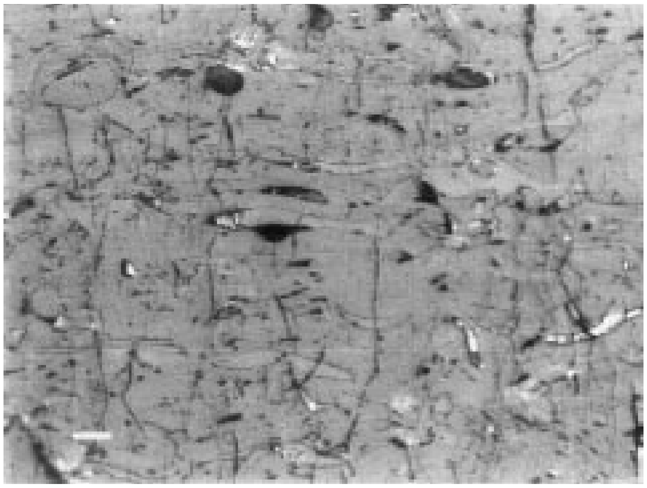

Fig. 18 Microstructure deposited at Ar/H_2 = 120/20 L/min, Z_p = 8 cm, Z_s = 22 cm, chamber pressure 200 Torr, and particle size −45 μm

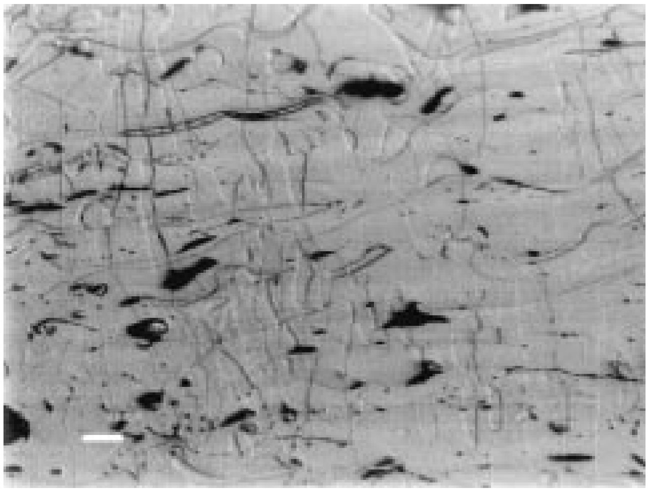

Fig. 20 Microstructure deposited at Ar/H_2 = 120/20 L/min, Z_p = 8 cm, Z_s = 22 cm, chamber pressure 200 Torr, and particle size −90 μm

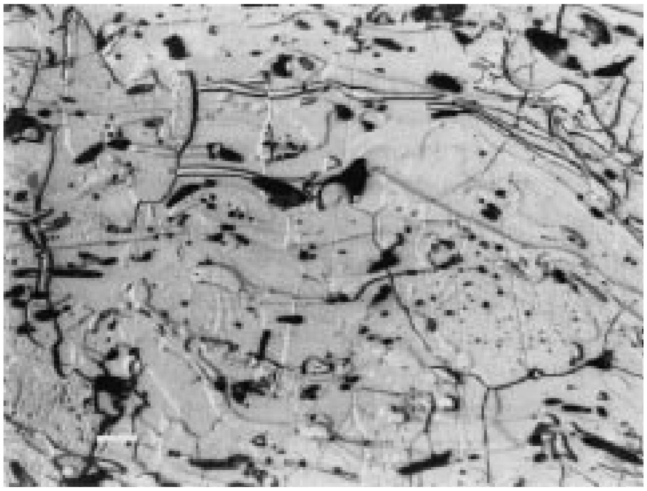

Fig. 19 Microstructure deposited at Ar/H_2 = 120/20 L/min, Z_p = 8 cm, Z_s = 22 cm, chamber pressure 200 Torr, and particle size −75 μm

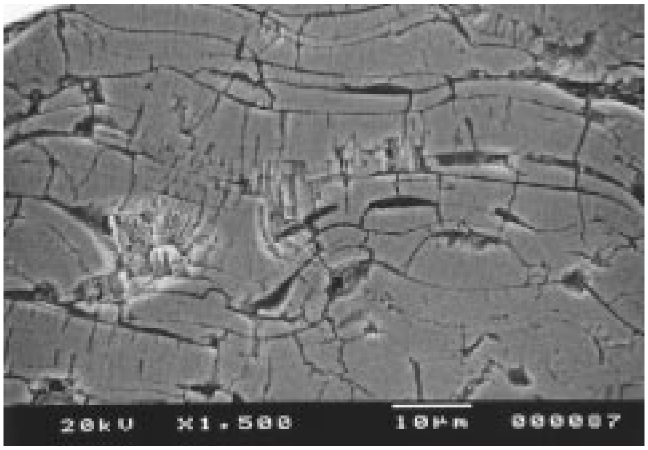

Fig. 21 Microstructure of the bottom part deposited at Ar/H_2 = 120/20 L/min, Z_p = 8 cm, Z_s = 22 cm, chamber pressure 200 Torr, and particle size −90 μm

distribution may also affect particle velocity and the radial spreading behavior as well as the surface roughness.[35] Three particle sizes, −45, −75, and −90 μm, were used. The other variables were fixed as Ar/H_2 = 120/20L/min, Z_p = 8 cm, and Z_s = 22 cm, and chamber pressure 200 Torr. The dimension of the columnar grain sprayed with −45 μm was 20 to 50 μm thick and 60 to 150 μm long, and the density appears to be high, as shown in Fig. 18. The lower part of the columnar grain was observed to be apiculate. This may result from fast heat removal downward due to good adhesion between layers. Good adhesion increases thermal diffusivity, so it acts as the heat sink. This sample shows comparatively uniform grain size. The dimension of the columnar grain sprayed with −75 μm particles was similar to −45 μm, but heterogeneous in grain size. This may result from particle temperatures lower than −45 μm; thereby, the temperature of the deposit was not high enough to accelerate the second stage recrystallization. The grain shape is a bell type, which is narrow on top and wide on the bottom, as shown in Fig. 19. This can also be explained by the heat removal rate, as shown above. The deposit density with smaller particles appears to be higher, as described previously.[36] The deposit with −90 μm powder shows grains 20 to 30 μm thick and 30 to 80 μm long. The microstructure of this deposit also shows a heterogeneous grain size, which may come from insufficient melting or heating due to the large size and result in incomplete recrystallization, as shown in Fig. 20. A cellular structure is observed in the thick bottom layer, as shown in Fig. 21.

Thickness and layer shape of the deposits vary widely with particle size. The thickness of the layers is 2 to 3 μm depending on particle size (refer to Section 3.3). Partially unmelted particles are discovered in −75 and −90 μm deposits, and furthermore, the layer of −90 μm deposit is not quite flat. In summary, the deposits sprayed with −75 and −90 μm powder exhibit a heterogeneous grain size and layer thickness increases with particle size. On the other hand, the deposit sprayed with

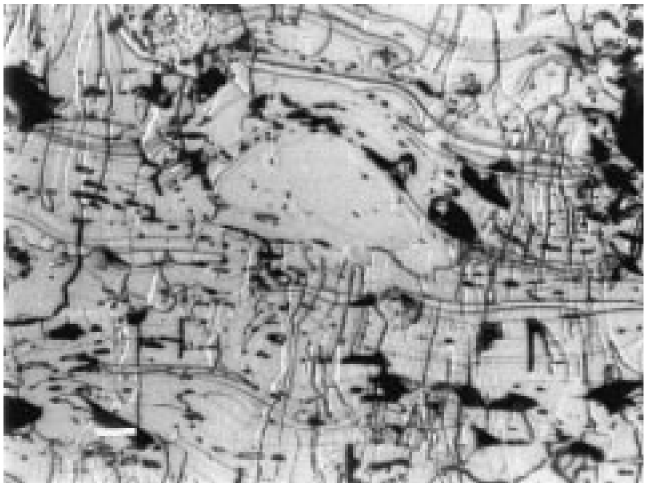

Fig. 22 Microstructure deposited at Ar/H_2 = 120/10 L/min, Z_p = 8 cm, Z_s = 22 cm, chamber pressure 200 Torr, and particle size –75 μm (deposited partially melted particle on center)

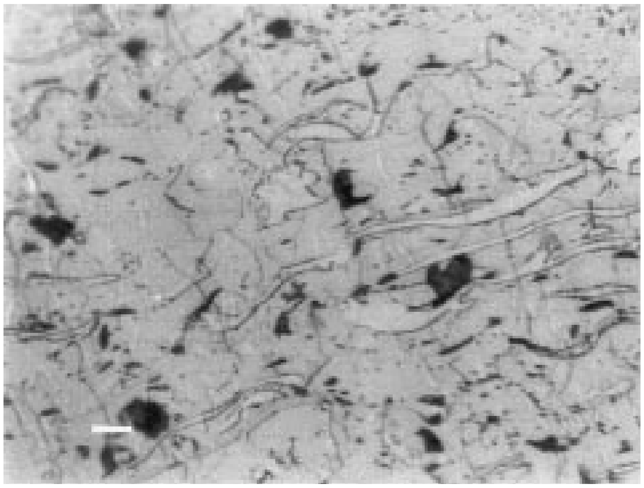

Fig. 23 Microstructure deposited at Ar/H_2 = 120/20 L/min, Z_p = 8 cm, Z_s = 30 cm, chamber pressure 200 Torr, and particle size –75 μm

–45 μm powder displays uniform grain size and a dense microstructure.

H_2 Gas Mixing Quantity. The H_2 gas flow rate was set to 20 or 10 L/min at a fixed Ar gas flow rate of 120 L/min. For the deposit with –75 μm particle size, the dimension and shape of the grains were similar at the bottom and lower middle parts regardless of H_2 gas mixing quantity. However, the deposit sprayed with 20 L/min of H_2 gas exhibited a larger columnar grain at the top and a thicker cellular structure at the chill part. There are many thin columnar grains and partially melted particles for coatings sprayed under these conditions, as shown in Fig. 22. This may be due to the limited grain growth with low temperatures and partially melted particles.

Splat shapes are also different with regard to the H_2 gas mixing quantity. For the condition of 20 L/min, splats are flatter, thinner, and wider perpendicular to the spraying direction. The splat shapes deposited with 10 L/min are not even. The main reason may be explained by plasma gas enthalpy. Higher H_2 gas mixing quantity gives higher plasma gas enthalpy and results in a higher temperature.[37] The tendency of the deposit with –90 μm is the same. For the condition of H_2 = 10 L/min, grain size is not homogeneous and a few partially melted particles were observed. The H_2 gas mixing quantity directly affects the plasma temperature. The temperature of the particles passing the higher enthalpy region is high. This heat contributes to grain growth. Therefore, deposits with the condition of Ar/H_2 = 120/20 L/min show a larger grain size. A thicker cellular structure in the chill part results from a lateral direction growth instead of a longitudinal orientation due to the poor contact between splats.

Spraying Distance. At the fixed condition of Ar/H_2 = 120/20 L/min, chamber pressure 200 Torr, probe position Z_p = 8 cm, and particle size –75 μm, powder spraying distance (Z_s) was varied between 22 and 30 cm from the bottom of the torch. The structures of the bottom and lower middle were similar for the two deposits' spray distance, regardless of Z_s. But for the other regions of coatings sprayed with Z = 30 cm, the thicknesses of the splats were irregular and agglomerated, as shown in Fig. 23. This indicates that the droplet may solidify during flight. For the –45 μm powder deposit, partially melted particles are frequently observed when the spray distance is 30 cm. This also arises from the solidification of particles during flight. Smaller sized particles are heated or cooled more rapidly than larger ones. In summary, particle temperature is kept higher when the spraying distance is 22 cm. This implies that particles are heated in the torch and then cool from their surfaces while passing through the plasma flame. This behavior arises from a higher heat flux potential at the torch rather than the plasma flame.[38]

Probe Position. The deposit characteristics were analyzed by varying the probe position in the plasma torch between 4 and 8 cm with fixed particle size, plasma gas content, and spray distance. Two deposits sprayed with –75 μm at different probe positions showed similar grain structure and chill structure on the bottom regardless of probe position. The grain size and splat thickness were heterogeneous at the condition of Z_p = 4 cm. In the case of the –45 μm deposit, there was no noticeable difference in the microstructure. In summary, probe position in the torch also affects the microstructure of the deposit. This indicates that the probe position also affects particle melting. But the influence of probe position on the microstructure was less severe than the other effects.

4. Conclusions

In the spheroidization experiment, designed and analyzed by ANOVA, H_2 gas mixing quantity affected the results of the spheroidization as much as 32%, and particle size as much as 25.3%. Therefore, a method to increase spheroidization is to increase the quantity of H_2 gas mixing. Interaction between the probe position and quantity of H_2 gas mixing was more effective than other interaction effects. Therefore, when altering the quantity of H_2 gas mixing is considered, altering the probe position should also be considered.

After melting, the particle kept its chemical composition homogeneously from center to surface, while the concentration was different from particle to particle. The degree of deformation of the droplet to splat was about 320%, and droplet thickness in the deposit varied between 2 and 3 μm depending on the deposition conditions. The yttrium concentration gradient of the interlayer boundary was linear in the range of 0.5 to 1 μm. The concentration profile at the grain boundary and chill showed neither yttrium concentration deviation nor segregation.

X-ray diffraction analysis and TEM micrograph showed that low yttrium content particles resulted in tetragonal phase in deposit.

The microstructure of the bottom part of the deposit showed small equiaxed or cellular grains. Equiaxed small grains prevailed when the droplets were quenched rapidly on substrate. Therefore, equiaxed small grains were mostly in the thin layers and cellular grains were in the thick layers. Many cellular grains were grown through the layers when they contacted and solidified with each other.

The lower middle part of a deposit showed poor adhesion and cracks. The middle part showed the largest columnar grain, 100 μm thick and 300 μm long, through the layers. Recrystallization prevailed in this part of the coating. The upper middle and top part of the deposit exhibited a heterogeneous grain size, but still showed strong adhesion between layers.

The deposition condition of Ar/H_2 = 120/20 L/min compared to Ar/H_2 =120/10 L/min results in larger grain size and thicker cellular in chill. Grain shapes were affected by the heat removal rate from the deposit to its surrounding.

The thickness and length of the columnar grain, shape of the grain, as well as thickness of the layers appeared to vary widely depending on the particle size. The deposit with −90 μm powder displayed heterogeneous grain size, which may come from insufficient melting or heating due to the large size and results in incomplete recrystallization. Splat shapes were affected by the quantity of H_2 gas when the Ar gas was fixed. For the condition of 20 L/min, splats were flatter, thinner, and wider perpendicular to the spraying direction. The splat shapes deposited with 10 L/min were not consistent in geometry. When powder was sprayed with Z_s = 30 cm, the thickness of the splats was irregular and agglomerated in comparison to Z_s = 22 cm. The influence of probe position on the microstructure was not as severe as the other effects.

Acknowledgments

This project was carried out under the Nuclear R&D Program by the Korean Ministry of Science and Technology. The authors thank Drs. M.I. Boulos and F. Gitzhofer for providing invaluable assistance throughout the plasma spraying experiment in Canada.

References

1. L. Pawlowski: *The Science and Engineering of Thermal Spray Coatings,* John Wiley & Sons, New York, NY, 1995, p. xv.
2. S. Sampath, R.A. Neiser, H. Herman, J.P. Kirkland, and W.T. Elam: *J. Mater. Res.,* 1993, vol. 8 (1), pp. 78-86.
3. E. Pfender: *Plasma Chem. Plasma Proc.,* 1999, vol. 19 (1), pp. 1-31.
4. S. Sampath, X.Y. Jiang, J. Matejicek, A.C. Leger, and A. Vardelle: *Mater. Sci. Eng.,* 1999, vol. A272, pp. 181-88.
5. S. Sampath: *Mater. Sci. Eng.,* 1993, vol. A167, pp. 1-10.
6. J. Jurewicz, R. Kaczmarek, and M.I. Boulos: *Radiofrequency Induction Plasma Deposition of Metals and Alloys under Reduced Pressure,* ICPS-7, ICPS, Eindhoven, Netherlands, 1985, pp. 1131-36.
7. X. Fan: Ph.D. Thesis, University of Sherbrooke, Sherbrooke, PQ, Canada, 1994.
8. X.L. Jiang: Ph.D. Thesis, University of Sherbrooke, Sherbrooke, PQ, Canada, 1994.
9. H.J. Matzke, V.V. Rondinella, and T. Wiss: *J. Nucl. Mater.,* 1999, vol. 274, pp. 47-53.
10. K.K. Srivastava, R.V. Patil, C.B. Choudhary, K.V.G.K. Gokhale, and E.C. Subbarao: *Trans. J. Br. Ceram. Soc.,* 1974, vol. 73 (3), pp. 85-91.
11. E.M. Levin, C.R. Robbins, and H.F. McMurdie: *Phase Diagrams for Ceramists,* American Ceramic Society, Columbus, OH, 1964, pp. 107, 141-42, and 163.
12. A. Vardelle, M. Vardelle, and P. Fauchais: *Plasma Chem. Plasma Proc.,* 1982, vol. 2 (3), pp. 255.
13. H. Herman: *MRS Bull.,* 1988, Dec., pp. 60-67.
14. X. Fan, F. Gitzhofer, and M.I. Boulos: *J. Thermal Spray Technol.,* 1998, vol. 7 (2), pp. 247-53.
15. R. Kingswell, K.T. Scott, and L.L. Wassell: in *Thermal Spray: International Advances in Coatings Technology,* C.C. Berndt, ed., ASM International, Materials Park, OH, 1992, p 421-26.
16. T.C. Nerz, J.E. Nerz, B.A. Kushner, A.J. Rotolico, and W.L. Riggs: in *Thermal Spray: International Advances in Coatings Technology,* C.C. Berndt, ed., ASM International, Materials Park, OH, 1992. pp. 405-13.
17. D.J. Varacalle, Jr., E. Acosta, J. Figert, M. Syma, J. Worthington, and D. Carrillo: in *Thermal Spray: Practical Solutions for Engineering Problems,* C.C. Berndt, ed., ASM International, Materials Park, OH, 1996, pp. 699-707.
18. D.C. Montgomery: *Design and Analysis of Experiments,* 4th ed., John Wiley & Sons, New York, NY, 1997, pp. 290-341.
19. P. Scardi and L. Lutterotti: *Surface Coating Technol.,* 1993, vol. 61, pp. 52-59.
20. C.A. Anderson, J. Greggi, Jr., and T.K. Gupta: in *Science and Technology of Zirconia II: Advanced in Ceramics,* N. Claussen, M. Ruhle, and H. Heuer, eds., The American Ceramic Society, Columbus, OH, 1983, vol. 12, pp. 80.
21. S. Sampath and H. Herman: *12th Int. Thermal Spraying Conf.,* London, June 4–9, 1989, paper no. 53.
22. C. Moreau, P. Cielo, M. Lamontagne, S. Dallaire, J.C. Krapez, and M. Vardelle: *Surface Coating Technol.,* 1991, vol. 46, pp. 173-87.
23. L. Pawlowski: *The Science and Engineering of Thermal Spray Coatings,* John Wiley & Sons, New York, NY, 1995, pp. 122-27.
24. C. Moreau, P. Cielo, and M. Lamontagne: in *Thermal Spray: International Advances in Coatings Technology,* C.C. Berndt, ed., *ASM International, Materials Park, OH,* 1992, pp. 761-66.
25. H. Bhat and H. Herman: *Thin Solid Films,* 1982, vol. 95, pp. 227-35.
26. W. Kurz and D.J. Fisher: *Solidification,* Trans Tech Publications, Aedermannsdorf, Netherlands, 1984, pp. 28-34.
27. F.J. Esper, K.H. Friese, and H. Geier: in *Science and Technology of Zirconia II: Advanced in Ceramics,* N. Claussen, M. Ruhle, and H. Heuer, eds., The American Ceramic Society, Columbus, OH, 1983, vol. 12, pp. 533.
28. L. Pawlowski: *The Science and Engineering of Thermal Spray Coatings,* John Wiley & Sons, New York, NY, 1995, pp. 139-46.
29. L. Pawlowski: *The Science and Engineering of Thermal Spray Coatings,* John Wiley & Sons, New York, NY, 1995, p. 160.
30. L. Pawlowski: *The Science and Engineering of Thermal Spray Coatings,* John Wiley & Sons, New York, NY, 1995, p. 128.
31. W.D. Kingery, H.K. Bowen, and D.R. Uhlmann: *Introduction to Ceramics,* 2nd ed., Wiley, New York, NY, 1976, p. 526.
32. L. Pawlowski: *The Science and Engineering of Thermal Spray Coatings,* John Wiley & Sons, New York, NY, 1995, p. 449.
33. Y.W. Kim, D.L. Bourell, and C. Persad: *Mater. Sci. Eng.,* 1990, vol. A123, pp. 99-115.

34. A.J.F. Craig and M. Hideaki: *Comput. Mater. Sci.,* 1999, vol. 14, pp. 177-84.
35. A.R. Nicoll and H. Eschnauer: *Proc. 11th Int. Thermal Spray Conf.,* Montreal, Sept. 8–12, 1986, pp. 289-99.
36. I.H. Jung, K.K. Bae, M.S. Yang, and S.K. Ihm: *Proc. 1999 US-Korea Materials Conf. (UKC),* Los Angeles, CA, Aug. 12–14, 1999.
37. M.I. Boulos, P. Fauchais, and E. Pfender: *Thermal Plasmas: Vol. 1,* Plenum Press, Elmsford, NY, 1994, p. 251.
38. L. Pawlowski: *The Science and Engineering of Thermal Spray Coatings,* John Wiley & Sons, New York, NY, 1995, p. 21.